LUND UNIVERSITY

FACULTY OF SCIENCE

# Self-assembly of Colloidal Perovskite Nanocrystals into Mesocrystals: An *In Situ* SAXS/WAXS Study

Robin Eriksson

Thesis submitted for the degree of Bachelor of Science
Project duration: 2 months

Supervised by Jesper Wallentin

Department of Physics
Division of Synchrotron Radiation Research
June 2024

# Abstract

This thesis investigates the self-assembly dynamics and structural characteristics of cesium lead bromide ($CsPbBr_3$) nanocrystals (NCs) into mesocrystals (MCs) using *in situ* Small- and Wide-angle X-ray Scattering (SAXS/WAXS) techniques. Central to this study is the exploration of the temporal evolution of mesocrystal formation and the associated superlattice peak-split due to the alignment of identical crystal planes between adjacent NCs. The self-assembly process was visualized in time and space by recording SAXS and WAXS signals while scanning the sample in a snake-like pattern. This method created detailed maps of the self-assembly process and allowed for real-time visualization through animations.

The study handles extensive datasets, with high-resolution scans generating data sizes up to 35GB, necessitating sophisticated data processing strategies to manage, analyze, and interpret the SAXS and WAXS measurements. These strategies included defining regions of interest to manage computational loads and developing scripts for effective data fitting and visualization. The research reveals that the distribution and spacing of NCs within MCs vary along the capillary, suggesting a density-dependent structuring that influences the mesostructure properties.

Significantly, this work contributes to a deeper understanding of the self-assembly mechanics of mesocrystal formation in lead halide perovskites, a subject that has not been extensively studied in real-time. The findings offer insights into the mechanisms driving NC assembly, that potentially could have an impact on the design and synthesis of perovskite-based materials in optoelectronics and other applications. Furthermore, the project highlights the effectiveness of SAXS and WAXS as tools for studying complex nanoscale transformations, setting a foundation for future research aimed at exemplifying the nuances of nanocrystal behavior *in situ*.

# Contents

# 1 Introduction

In recent years, the field of material science has witnessed significant advancements due to the synthesis and characterization of novel nanomaterials. Among these materials, lead halide perovskite nanocrystals (NCs), particularly cesium lead bromide ($CsPbBr_3$), have attracted substantial attention due to their remarkable optoelectronic properties and their versatility in applications ranging from solar cells to light-emitting devices. This thesis explores the self-assembly of $CsPbBr_3$ NCs into mesocrystals (MCs), a process facilitated by a solvent-antisolvent diffusion method using hexane and perfluorodecalin, respectively. The NCs are stabilized by a mixture of short-chain decylamine and long-chain oleic acid ligands, which play a role in their assembly behavior and the resulting mesostructure properties.

Fig. 1.1 illustrates the general idea of the NCs self-assembly into MCs and the basic role of the ligands, as well as real life images of the two different crystals with related length-scales.

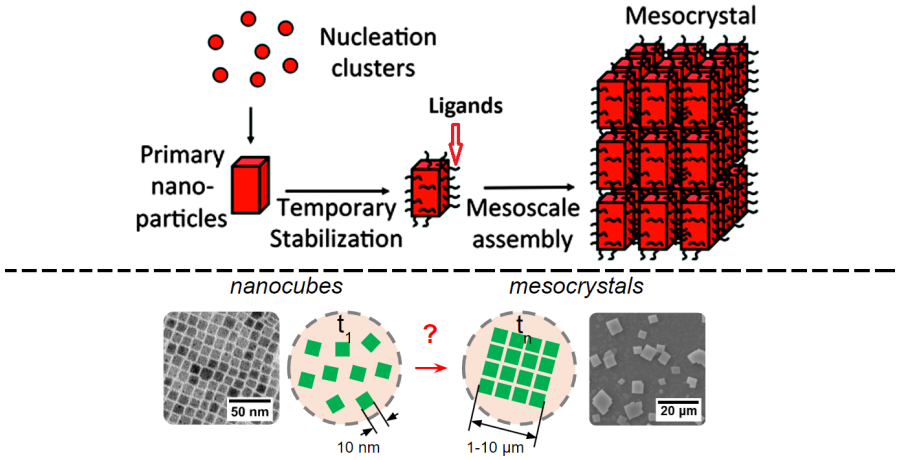


Figure 1.1: General illustration of the self-assembly process of NCs into MCs (upper image), and real example of the NCs and MCs with related length-scales (lower image). The self-assembly process from NCs to MCs as seen in the lower part of the image, or last step in the upper part, is what is studied in this report. The upper part is taken from Elena V. Sturm and Helmut Cölfen Fig 1, and modified [1]. The lower part is reproduced with modifications from the experimental report for Max IV standard proposal no. 20230363 and provided by courtesy of Dr. Dmitry Baranov, Division of Chemical Physics and NanoLund, Lund University.

The ability of $CsPbBr_3$ NCs to form ordered mesostructures such as MCs results in unique properties both from the individual NCs, but also as a collected group of said crystals. The study of these MCs provides important information about their crystalline and superlattice structures, directly influencing their electronic and optical functionalities. And by understanding the assembly process better we can learn to optimize the material in order to further develop new technologies, such as light-emitting devices or solar cells as previously stated.

The primary aim of this thesis is to examine the growth dynamics and structural character-

istics of $CsPbBr_3$ NCs as they self-assemble into MCs. This involves an analysis of the crystalline structures using *in situ* Small- and Wide-angle X-ray Scattering (SAXS/WAXS), techniques that offer nanoscale resolution and the ability to capture real-time structural transformations. Another key objective includes improving the handling of large-scale data obtained from beamline measurements, processing this data, and extracting critical information for analysis. Additionally, this study focuses on investigating the superlattice Bragg peak-split, which occurs due to the alignment of identical crystal planes between adjacent NCs within the MCs, providing further insight into the structural ordering during the self-assembly process.

The experimental work was conducted at the MAX IV synchrotron facility in Lund, using the ForMAX beamline that utilizes the advanced Eiger and Lambda detectors to capture high-resolution SAXS and WAXS data. This thesis describes the sample preparation, data gathering, including the azimuthal integration technique, crucial for the analysis of diffraction patterns, and the analytical methods employed to understand the evolution from individual NCs to complex MC assemblies. The SAXS data, gathered using the Eiger detector, provides information about the overall size and distribution of NCs and MCs, while the WAXS data, obtained with the Lambda detector, provides detailed information on the crystalline structure. Together, these techniques complement each other, presenting a fuller picture of the nanoscale to mesoscale transition in perovskite materials.

This study not only helps us understand the $CsPbBr_3$ NCs behavior and MCs formation but also shows the capabilities of x-ray scattering techniques in complex nanostructures. The results of this study will have an impact on the design and synthesis of next-generation materials, helping in the development of new applications in different scientific fields, including the field of optoelectronics.

# 2 Theory

## 2.1 Perovskite nanocrystal-growth into mesocrystals

### 2.1.1 Perovskites

The perovskite structure following the $ABX_3$ formula for two positive ions A and B (usually of different sizes), and three negative ions X, was first found in 1839, see Figure 2.1 A). A subgroup of these perovskites is the metal halide perovskites (MHPs), who began gaining attention in the scientific community around the beginning of 1990s for their fascinating properties in optical and electronic components, such as high absorption coefficients, tunable bandgaps and high charge carrier mobility's.

The different positions for the elements/molecules are called sites as seen in fig. 2.1 A). The ABX-sites of MHPs are commonly filled with the following elements/molecules:

- A: caesium, methylammonium, formamidinium
- B (the metal): lead, tin
- X (the halogen): iodine, bromine, chlorine

Because of the wide range of possible combinations of ions, the resulting MHPs have very

tunable properties, such as colors of the emitted light as seen in fig. 2.1 C).

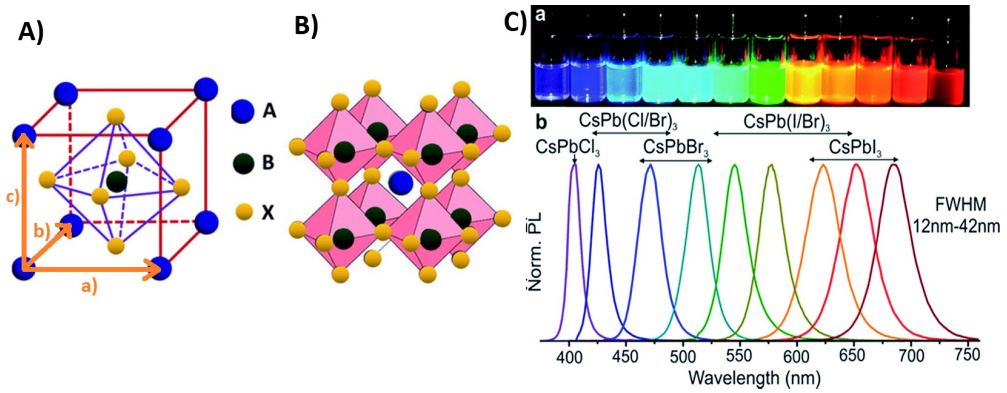


Figure 2.1: A) The perovskite crystal unit cell with its lattice parameters a, b and c, where if $a \neq b \neq c$ would result in an orthorhombic unit cell. B) The extended unit cell showing the full MHP crystal structure. C) The tunable emission of perovskite nanocrystals showing the distinction between the different element combinations in the MHP. Images A) and B) taken from [2] and modified, C) taken from [3].

### 2.1.2 Crystalline structure of solids

To understand and make use of the perovskite structure, one would first need to look into the crystalline structure of solids described by lattices. The crystal lattice can be described as a three-dimensional arrangement of points that define the periodic array in which the particles are situated. Each point in the lattice represents the position of a particle (atom, ion, or molecule) as was seen in fig. 2.1 A), and is known as a lattice point.

A "Bravais" lattice is a set of points constructed by translating a single lattice point in discrete steps according to a lattice vector such as

$$\vec{R} = n_1\vec{a}_1 + n_2\vec{a}_2 + n_3\vec{a}_3, \tag{2.1}$$

where the $n_i$ are any integers, and $\vec{a}_i$ are primitive vectors, which lie in different directions and span the lattice [4]. In three-dimensional space, the complex arrangement of atoms, ions and molecules in crystalline materials is defined by one of 14 distinct Bravais lattices. They are in turn organized into seven crystal systems: cubic, tetragonal, hexagonal, orthorhombic, monoclinic, triclinic and trigonal, which further fall into four types of lattice configurations: primitive, body-centered, face-centered and base-centered.

For each of these configurations a basis can be described as the arrangement of one or more particles at each lattice point. This unit is essential for understanding how the repeating patterns of a crystal's structure emerge from the translation of the smallest repeating block, known as a primitive unit cell, along lattice vectors. These lattice structures and their bases give rise to a diversity of crystal structures, categorized into 230 space groups. This categorization shows the versatility of crystal arrangements, enabling the same structure to show

vastly different properties based on the orientation of its atoms. Such orientations can lead to structures being either centrosymmetric, where they possess a center of symmetry, or non-centrosymmetric, lacking such a center, thereby influencing the material's physical properties.

The reciprocal lattice $\vec{G}$ is the Fourier transform of another real lattice such as the Bravais lattice, $\vec{R}$, which is commonly used for crystal systems. It is expressed accordingly,

$$\vec{G} = hb_1 + kb_2 + lb_3, \tag{2.2}$$

where h, k, and l are integers while $\vec{b}_i$ are the vectors of the reciprocal lattice. The key characteristic of $\vec{G}$ being a Fourier transform of $\vec{R}$ is shown by the equation $\vec{R}\cdot\vec{G} = 2\pi n$, where n is an integer. This relation is essential for the reciprocal lattice's role in identifying the planes with Bravais lattices using Miller indices. These planes, which intersect the crystal axes at integer multiples of the lattice constants (potentially extending to infinity), are defined by inverting these intersection multiplies $\left(\frac{1}{n_1}, \frac{1}{n_2}, \frac{1}{n_3}\right)$ and adjusting them to integer values, resulting in the Miller indices (h, k, l). Miller indices hence gives us the normal of the reciprocal plane and serve as a standardized method for describing the orientation and position of these lattice planes, which are a fundamental aspect of all crystalline solids.

The fundamental distinction between reciprocal space and real space lies in their inverse relationship regarding length scales. A longer distance in real space (which corresponds to the distance between planes in a crystal), translates into a shorter distance in reciprocal space, and vice versa. This inverse relationship is particularly important in diffraction studies. Different diffraction methods are commonly used when identifying crystal structures, where high-angle diffraction peaks (which occur at larger values of reciprocal space coordinates) correspond to closely spaced lattice planes in real space. Conversely, low-angle peaks indicate more widely spaced planes. This principle allows for the determining of the structure of the crystal from its diffraction pattern.

### 2.1.3 Nanocrystals

With a sophisticated synthesis process usually involving ligands (molecules which constrain crystal growth), the bulk of MHPs can be controlled and transitioned into perovskite nanocrystals (NCs) by down-scaling the size of the material into nanometer range. This can be accomplished by utilizing the quantum confinement effects, where the size of the crystal is reduced to approximately the wavelength of the electrons' wave function. This leads to an increase in the band gap energy, and thus alters the absorption and emission spectra. The optical and electronic characteristics of the material can be tailored by the shape and size of the nanocrystals making it possible to grow nanostructures such as nanoplatelets, nanosheets, nanowires and quantum dots.

The NCs can be considered as multiple unit cells stacked together in three dimensional space into for example a cubic shape to form a crystal structure. In the case of the Lead Halide Perovskite (LHP) such as the orthorhombic $CsPbBr_3$ defined by the a, b and c lattice parameters of different lengths, in general, the orientation of the orthorhombic unit cell is identical for every individual NC, forming perfect crystals. There are possibilities where the

unit cells in a single NC are not perfectly aligned and thus forming so called ”domain walls” in the crystal where for example the ”a” parameter is parallel to ”c” instead of itself, forming a barrier in the crystal. This is generally not energetically favorable as misalignment's tend to introduce higher energy states due to increased strain and instability within the crystal, and crystals are generally stable when they maintain a high degree of symmetry. Therefore such alignments only occurs under certain circumstances, such as in nanowire growth, but for the general NC formation they are regarded as perfect crystals.

### 2.1.4 Growth into mesocrystals

Under certain conditions, some described in Toso et al. [5], NCs can organize themselves into a mesocrystalline structure as was seen in fig. 1.1. This structure is characterized by a multitude of tiny crystals, each bearing a somewhat uniform shape and size that are periodically positioned. These crystals are aligned along the same crystallographic axes while maintaining a distinct space between each other. This type of organization can be called oriented aggregation or oriented attachment, a phenomenon that results in the crystals being parallel to one another in their crystallographic orientation while being physically separated.

In the orthorhombic $CsPbBr_3$ NCs, where one side, denoted as ”c”, is slightly elongated along its axis, while the other two sides ”a” and ”b” might be of similar but not identical lengths. The ”a” side of one NC may easily align with the ”b” side of the another NC within the mesocrystals (MCs) because of their similar size, hence the exact alignment of the NCs becomes more complex and challenging to determine. Therefore, for practical reasons, it is assumed that the orientations of the axes are parallel for all NCs within a specific MC. While on the larger scale, a sample containing many different MCs may very well be arbitrarily oriented depending on the circumstance of the growth, such as the the substrate surface.

The assembly of nanocrystals (NCs) into mesocrystals (MCs) can occur through two primary methods. One method is directed assembly, where external forces are used to guide the organization of NCs. Alternatively, NCs can undergo self-assembly, a simpler process that may involve a solvent-antisolvent diffusion method. In this method, NCs are dispersed in a solvent like hexane and then introduced to a denser antisolvent such as perfluorodecalin. As the solvent and antisolvent begin to intermix at the interface where their densities converge, the NCs naturally align and gradually form a mesocrystalline structure. This is shown and described in more detail later in section 2.3. The self-organization is driven by various forces and interactions, including capillary and Van der Waals forces, and potentially magnetic or electric interactions, depending on the specific conditions of the experiment.

The resulting properties of the mesocrystals can differ depending on the NCs. In the case of perovskite NCs, the mesocrystal properties involves characteristics such as enhanced photovoltaic performance, controlled bandgap tunability and enhanced light absorption and emission. Many different properties of ordered nanocrystal superlattices are discussed in Boles, Engel and Talapin [6].

## 2.2 X-ray diffraction

In order to study nano-sized crystals and their structures, we employed x-ray diffraction (XRD) methods. XRD is a powerful analytical technique used for finding the atomic and molecular structure of a crystal. When a beam of x-rays, which are electromagnetic waves (EM) hits a crystal, it interacts with the periodic electron densities of the crystal lattice and scatters in many specific directions. From these scattered angles and the diffraction intensities at these angles, structural properties such as the arrangement of atoms within a unit cell, crystal lattice symmetries and parameters, even molecular structures can be found.

X-rays interacts weakly with matter resulting in them only scattering either once or not at all, which is also beneficial in air filled environments as are commonly used for these kinds of experiments because of simplicity. The weak interactions provides direct information about the path and structure that the x-rays encounters, and thus resulting in more accurate measurements. Additionally, when these EM waves travels for a long enough distance they can be considered plane waves as they hit the sample, hence why the sample and detectors usually are placed further away from the source. This then give rise to the foundational equation in x-ray diffraction, Bragg's law which predicts the angles at which diffraction will occur for a crystal lattice according to:

$$n\lambda = 2d\ sin(\theta), \tag{2.3}$$

where the integer n is the order of the reflected wave, $\lambda$ is the wavelength of the incident x-ray, d is the distance between the crystal planes and $\theta$ is the angle of the incidence at which the x-rays strike the crystal plane. This concept can be seen in lower section of fig. 2.2, where the incoming waves scatter at the atomic or crystalline planes and form constructive interference for rays following Bragg's conditions.

The upper section of the fig. 2.2 shows the relation between the wave-vector $\vec{k}$ (parallel to the incoming x-ray) and the reciprocal lattice vector $\vec{G}$ from eq. 2.2 of the normal to the plane of the crystalline structure described by the Miller indices (hkl). The relation between the wavelength $\lambda$ of the incoming wave is also shown as $k = 2\pi/\lambda$.

### 2.2.1 Small- and Wide-angle X-ray Scattering (SAXS/WAXS)

When doing XRD, the scattered x-rays can form ring-like diffraction patterns which can be measured on one or multiple detectors at the same time. A powerful combinations for this is the small- and wide-angle x-ray scattering (SAXS/WAXS) method, which utilizes both the rays scattered at the small and wide angles and thus contains different valuable information about the crystal structure. The range of angles for each method may differ depending on the photon-energy source, like a synchrotron beamline. Commonly, angles above 5-10 degrees are considered for the WAXS-range, while for angles below the SAXS ranges.

(1) The WAXS-method has many similarities to powder XRD in the sense that both produce patterns with peaks at specific angles that corresponds to the distances between planes of atoms or molecules in the sample, following Bragg's law. The wide angles corresponds to smaller interatomic spacing that ranges between 0.1 nm to a few nanometers, where the position of the diffraction-peaks at the angles corresponds to the Bragg planes of the crystal

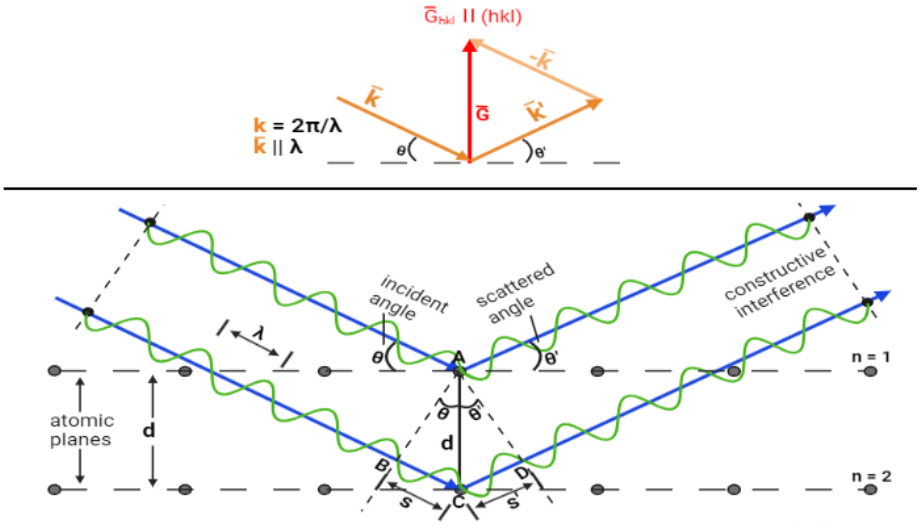


Figure 2.2: Lower section of the image illustrating the Bragg conditions in eq. 2.3 for an incoming wave scattering on two atomic planes. Upper section showing the k-vector's relation with the incoming wave, and the reciprocal lattice vector $\vec{G}$ with the same alignment as the normal to the plane, defined by the Miller indices (hkl).

structure while the symmetry and distribution of peaks can provide clues about the crystal lattice symmetry.

A variation of the WAXS technique is scanning WAXS (SWAXS). In SWAXS, either the sample or the detector is systematically moved in a series of positions or angles. This allows for a more thorough scanning of the sample with possibly a smaller beamsize, resulting in more detailed data being gathered of the sample for many smaller points and thus showing the smaller changes, while still being able to cover the whole area. In comparison to using a large beamsize that covers the whole sample which would give a more general view of the sample as a whole. This alternative scanning method is useful when analyzing complex materials with greater accuracy, providing a wider range of detailed data than what is achieved with a stationary scan, which is very suitable for in situ experiments where very small changes can occur in arbitrary places in the sample.

(2) The SAXS method provides statistically averaged structural data across a large sample volume. This characteristic makes SAXS highly effective for real-time, *in situ* structural analysis during dynamic processes, such as chemical reactions. Consequently, a setup that integrates both scanning WAXS and scanning SAXS simultaneously can be beneficial for comprehensive *in situ* analysis, as it combines the detailed atomic structural information from WAXS with the broader crystal or molecular spatial information from SAXS.

In both methods, the scattered intensity is represented as a function of the scattering vector q defined by,

$$q = \frac{4\pi}{\lambda} sin(\theta), \tag{2.4}$$

commonly measured in the units of $Å^{-1}$, where $\theta$ is half of the scattering angle (defined by $2\theta$) and $\lambda$ is the wavelength of the x-rays.

SAXS is used for probing structures typically at 1-100 nm ranges by studying the intensity of the x-rays scattered at very small angles. The SAXS signal generally is considered for $q < 10nm^{-1} = 100Å^{-1}$ [7], and thus provides information of the shape and size of both crystalline and noncrystalline nanoparticles or macromolecules, often giving information on the size distribution and spatial arrangement within the sample. In the case of LHP NCs forming MCs, SAXS would scatter on the NCs in a MC in a similar way as WAXS would scatter on the atoms in the planes of a single crystal. Hence SAXS could be used to find the distance between the NCs in the MC structure.

The inverse relationship between the position of the peak in the scattering pattern and the periodicity or size of the structure in real space is given by,

$$d = \frac{2\pi}{q}, \tag{2.5}$$

indicating that larger structures scatter at smaller angles. More on SAXS can be found in chapter. 4 of Oliver H. Seeck and Bridget Murphy [7].

## 2.3 The Lead Halide Perovskite superlattice

When studying lead halide perovskites such as $CsPbBr_3$, formed into NCs, the SAXS and WAXS methods are very useful for structural analysis, especially when they are grown into mesocrystals as previously mentioned. An example of this can be seen in fig. 2.3, showing a setup of how the individual NCs over a certain time-frame align into mesocrystalline structures, also commonly known as superlattices (SLs), and how the *in situ* detection method for this could look like.

When probing the atomic planes of LHP NCs, depending on if they are arbitrarily orientated such as the pre-assembly phase, or if they have formed a mesocrystalline superstructure, the resulting Bragg-peaks from the interference might look different. Fig. 2.4 illustrates the difference between XRD on a SL and randomly oriented NCs, where for the SL, a peak-split occurs contrary to the case with the unstructured NCs. The figure also shows the relation for the split according to

$$n\lambda_{x-ray} = 2\Lambda sin(\theta), \tag{2.6}$$

for the SL-period $\Lambda$ which is the distance between the center of two superstructured NCs, and the order of satellite (SL reflections) n. This can, similarly to eq. 2.5, be used to calculate the corresponding peak center as $q_n = 2\pi n/\Lambda$, obtained by rearranging eqs. 2.4 and 2.6. For $CsPbBr_3$ NC samples similar to the one used in Toso et al. [5], SL splits should occur at $q \approx 1.08\ Å^{-1}$ and potentially at even higher angles such as $q \approx 2.15\ Å^{-1}$. For better ordered samples the multilayer diffraction could potentially be seen more clearly at higher angles.

The reason for the possibility to observe splits is, as eq. 2.6 explains, that the ligand molecules makes the NCs orient themselves at a small distance between each other. And similarly to the constructive Bragg interference as was seen in fig. 2.2 that occurs between lattice planes in

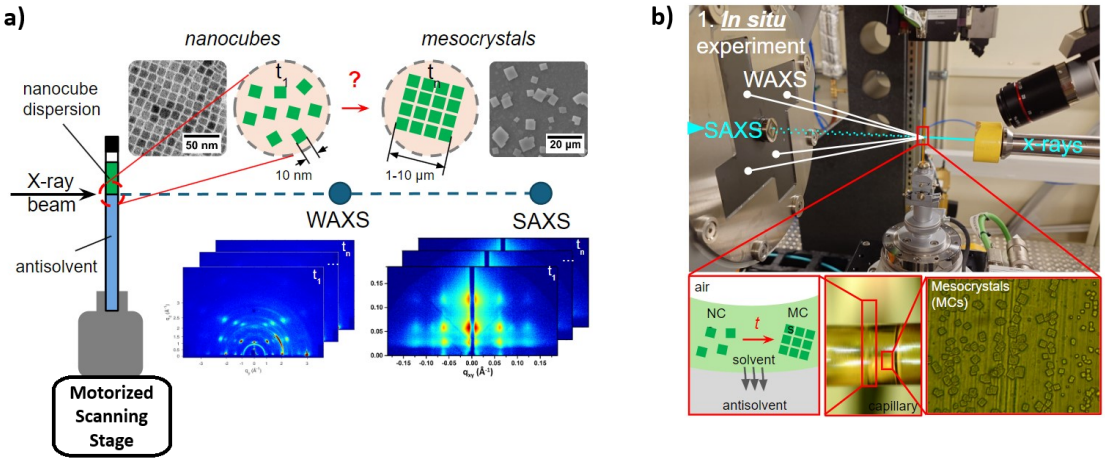


Figure 2.3: An example setup of an *in situ* experiment using SWAXS in order to study the self-assembly process of LHP NCs into MCs using solvent-antisolvent diffusion. a) showing a theoretical setup with example diffraction patterns. b) showing a real life setup and an illustration of the process. These image are reproduced with modifications from the experimental report for Max IV standard proposal no. 20230363 and provided by courtesy of Dr. Dmitry Baranov, Division of Chemical Physics and NanoLund, Lund University.

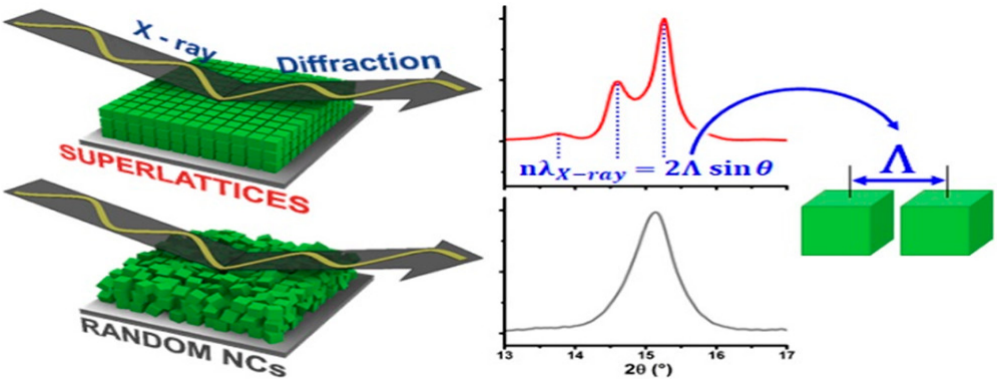


Figure 2.4: Comparison of x-ray diffraction patterns from Lead Halide Perovskite nanocrystals. The top part displays diffraction from a mesocrystalline superlattice, showing a split Bragg peak with the related eq. 2.6. The bottom part shows diffraction from randomly oriented nanocrystals, resulting in a single Bragg peak. Image taken from Toso et al. abstract figure [5].

the same crystal, when instead multiple NCs such as the orthorhombic $CsPbBr_3$ are aligned and thus have parallel lattice parameters, constructive interference can occur between the identical crystal planes of different NCs. The result is the split of the Bragg with a small shift between two peak-tops equal to the distance between the two identical crystal planes in ad-

jacent NCs. It is important to note that these are not two individual constructive interference peaks from the NC-planes individually, as that would only result in one single Bragg peak of just higher intensity. But instead it is the constructive interference between the two interfering waves from one NC as was seen in fig. 2.2, and the two waves in the next NC in the MC, with a spacing $\Lambda$ between two identical planes in the two NCs. Very similar to d in in a single NC, but for the MC instead.

# 3 Experimental Setup & Method

## 3.1 Sample preparation

The $CsPbBr_3$ perovskite NCs used in this report were synthesized at the Italian Institute of Technology, Genova, Italy, by a hot-injection method as described in Toso et al. [5] with modifications. The modifications consisted in replacing long-chain oleylamine (C18) ligand with shorter chain decylamine (C10) ligand. The nanocrystals have orthorhombic structure, with unit cell crystal structure parameters that are based on the published Rietveld refinement: a = 8.2248 Å, b = 8.2741 Å and c = 11.7748 Å [5]. The NCs are assumed to have cubic shape with specified edge lengths of 7-8 nm from transmission electron microscopy characterization, and were covered by a mixture of shortchain decylamine (C10) ligands and long-chain oleic acid ligands, to be described in the paper in preparation, Filippi et al. [8]. For the *in situ* mesocrystals growth, nanocrystals were dispersed in hexane.

The *in situ* growth of mesocrystals was performed by using solvent-antisolvent diffusion approach for self-assembly of perovskite nanocrystals in similar fashion as in Baranov et al. [9]. In that approach, hexane acts as a solvent, and perfluorodecalin acts as an antisolvent in the solvent-antisolvent diffusion process. For the synchrotron experiment, the growth was carried out in Kapton capillaries. The Kapton capillary was first filled with the perfluorodecalin antisolvent, followed up by an a thin interlayer of the neat hexane solvent before deposition of the NC-hexane dispersion on top. The thin interlayer was used to prolong the diffusion time before the NCs could start the assembly process, since 3-5 minutes were needed to activate the beamline and initiate the measurement after the sample was manually mounted into the sample holder. The Kapton was chosen because of its low x-ray scattering background signal and chemical resistance to organic solvents.

## 3.2 ForMAX beamline and detectors

The ForMAX beamline at the MAX IV synchrotron facility in Sweden is designed for in-depth structural characterization of materials on scales from millimeters down to nanometers. This is achieved through advanced imaging techniques such as full-field tomographic imaging, small- and wide-angle x-ray scattering (SAXS/WAXS), and scanning SAXS/WAXS imaging, all integrated within a single instrument. The beamline operates within an energy range of 8-25 keV, and can adjust the beam size at the sample between approximately 1$\mu$m to 1mm. Full details about the beamline can be found on the MAX-lab website [10].

Beamline staff assisted in optimizing sample-detector distance, the x-ray energy (14.31 keV) and the beamsize (50x50 $\mu m^2$), in order to capture the SAXS/WAXS q-ranges of inter-

est which was 0.006-0.28 $Å^{-1}$ and 0.67-3.4 $Å^{-1}$, respectively. A capillary containing a sample could then manually be mounted on a translation-able and rotatable experimental stage close to the WAXS windmill detector (lambda), see example setup fig. 2.3 b). The scanning range and the final resolution could be determined when running the scans, as well as how the scanning process would be made. For the data used in this report, a so called "snake-pattern" was used, where the stage moved the sample through the beam as the name suggests. Pre- and post-assembly scans was made for higher resolution images of (51, 240) 12240 pixels over a 2.5x6 mm range with step sizes $50\mu m$ and $25\mu m$ respectively (x,y), while for the *in situ* scans a lower resolution was used of (81, 50) 4050 pixels over a 2x5 mm range with step sizes $25\mu m$ and $100\mu m$ respectively.

### 3.2.1 Eiger and Lambda detectors

The two detectors used for the SAXS/WAXS methods at the ForMAX beamline are called Eiger (SAXS) and Lambda (WAXS). The Dectris EIGER2 X 4M SAXS detector was at the moment placed on a motorized XYZ trolley inside the 9m long SAXS flight tube where the sample to detector distance could be varied between approximately 0.8 and 7.6 m. The custom-designed X-Spectrum Lambda 3M WAXS detector was mounted on the front of the SAXS flight tube and the four detector-components of the WAXS detector had the geometry of a ”windmill” with a central hole, to allow for the direct beam and the SAXS signal to pass through [10], once again visible in fig. 2.3 b). The 4M and 3M in the detector names represents the number of pixels (Mega/million) for the sensors, with pixel sizes 75x75 $\mu m^2$ and 55x55 $\mu m^2$ as well as maximum frame rates of 500 Hz and 1 kHz for the Eiger and Lambda detectors respectively.

## 3.3 Azimuthal integration

Azimuthal integration is a method used in x-ray scattering techniques such as SAXS/WAXS, to convert 2D scattering patterns into 1D intensity profiles. Full description of the method can be be found in Jensen et al., 2022 [11]. In short summary, it takes the pixel coordinates of the scanned point from the 2D detector data and through integration converts them into polar coordinates ($2\theta$, $\chi$). The azimuthal angle $\chi$ around the beam direction representing the orientation of scattered intensity, and scattering angle $2\theta$ is commonly converted to the scattering vector length q by the relation in eq. 2.4.

As the beam is aligned with the sample and the detector, a PONI (Point Of Normal Incidence) is used as a reference point relative to each pixel coordinate. The related geometry of the setup can be seen in fig. 3.1, showing related parameters which were saved in a PONI-file and used for the integration. This is also illustrated with real raw data as seen in fig. 3.2, showing the diffraction pattern to the left on the detector, similar to fig. 3.1 but with a centralized beam, while the cake plot is shown to the right for the azimuthal angle $\chi$ over the scattering vector q.

## 3.4 Data gathering, processing and analysis

At ForMAX, once the beamline instruments were calibrated, multiple measurements were performed on various samples. *In situ* scans (numbered 1155-1181) monitored the self-assembly

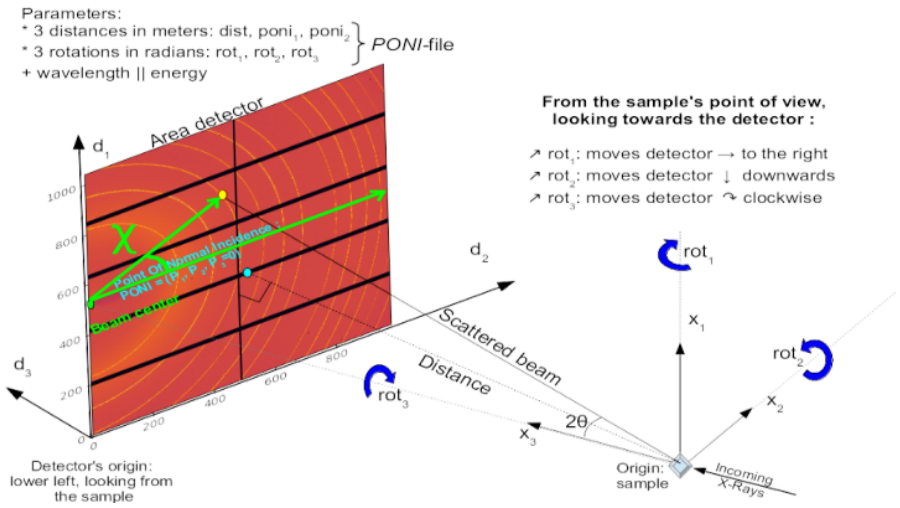


Figure 3.1: The geometric setup used to produce a PONI-file for the Azimuthal Integration at the ForMAX beamline. Image taken from PyFAI and modified [12].

of $CsPbBr_3$ nanocrystals (NCs) into mesocrystals (MCs), conducted at specified intervals. Additionally, two comprehensive maps were completed before and after the assembly process (scans 1187 and 1186, respectively), with the pre-assembly scan conducted on a replica sample following the main assembly.

For each scan, the dimensions of the scanned sample area and the resolution were determined as previously mentioned in section 3.2. Each scanned point (or pixel) either displayed a diffraction pattern or did not, depending on whether the beam encountered the targeted crystal structure. Fig. 3.2 illustrates examples of a raw and thus pre-processed scanned pixel from the post-assembly sample, showcasing diffraction patterns in both 1D data and a 2D cake-plot format.

The raw data from the scanning SAXS/WAXS was automatically processed by an azimuthal integration script at the beamline, which resulted in immediately usable 1D and 2D (cake) processed data with converted q-values, thereby eliminating the need for manual handling. A simple script, provided by the beamline, allowed for the loading of this processed data for any of the scans. And with some minor modifications of the given script, each frame for a selected scan could be integrated, summed up, and reshaped to facilitate the mapping of the capillary as well as to produce integrated plots for both the 1D and 2D data, providing an overview of the sample's characteristics. A region of interest (ROI) in the data was chosen for the integrated plots as seen in fig. 3.3 for WAXS, showing the second ordered peak split. This was done similarly for the SAXS data, which in turn could be used for further analysis described in the following sections.

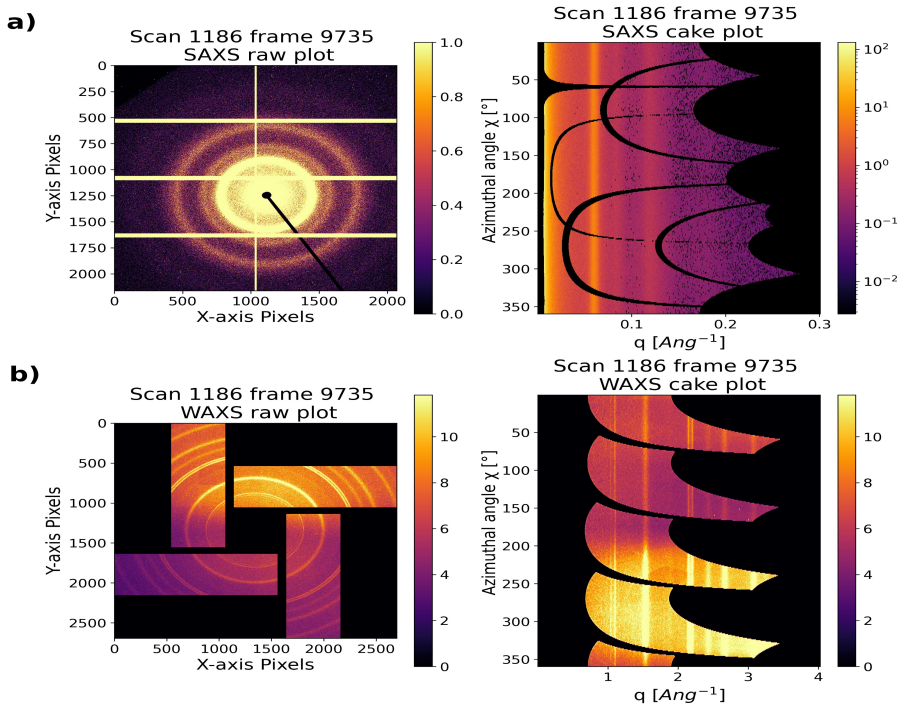


Figure 3.2: SAXS/WAXS example plots of the raw data from the post-assembly scan 1186 for the 9735 scanned pixel. Both a) and b) shows diffraction patterns, where a) is from the Eiger detector and b) is from the ”windmill” Lambda detector.

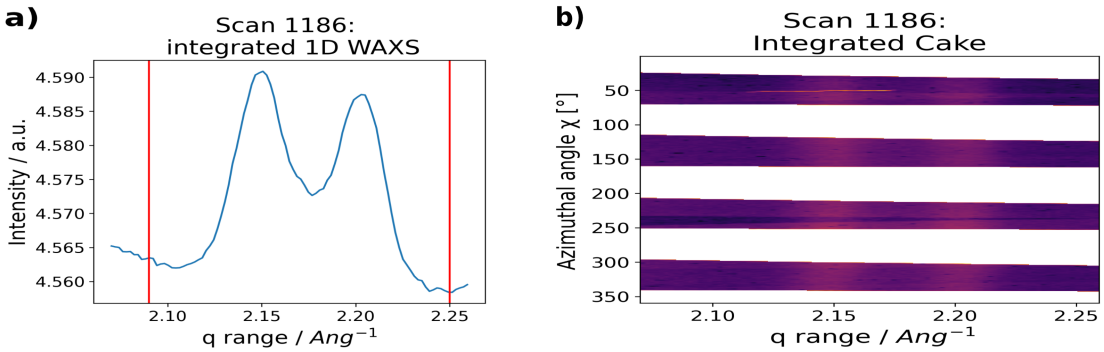


Figure 3.3: Processed WAXS data from post-assembly scan 1186, showing a) the 1D plot of the logarithmic sum of all pixels, displaying the second ordered SL split around the ROI range 2.09-2.25 Å$^{-1}$; b) the 2D integrated cake plot for the azimuthal angle, showing increased intensity at the same q-range as the peaks in the 1D plot.

### 3.4.1 Real position analysis

The script designed to map the capillaries in real space and analyze the self-assembly of the LHP NCs required performing Gaussian fits on spectral peaks through several difficult steps.

The process began by manually examining and selecting individual frames (pixels), identifying them based on different peak characteristics such as smaller, larger, and absent peaks. This step was crucial as frames often contained random noise spikes. This preliminary manual selection was essential to develop a Gauss-fitting script adaptable to varying datasets, which could include anywhere from 4000 to 12000 frames, stressing the importance of an automated approach.

Background noise was typically accounted for and eliminated using a straightforward linear fit. However, some datasets from the SAXS scans required a second-degree polynomial fit due to the different noise patterns in the data. To further refine the data, a "gliding averaging" technique was employed to smooth out datasets with scattered points, a common issue with low-intensity peaks. The subsequent challenge involved addressing random spikes frequently appearing in arbitrary frames and positions. A function was developed to calculate the derivatives between two adjacent points across all data points. This function was tested on various frames exhibiting different peak types to establish a general threshold for the derivatives. This threshold was critical to effectively filter out spike points without excessively removing data points vital for maintaining the accuracy of the Gaussian fits, particularly in scenarios involving normal peaks with steep slopes.

For illustration, see fig. 3.4, which shows an example of a challenging low-amplitude peak affected by double-spike noise.

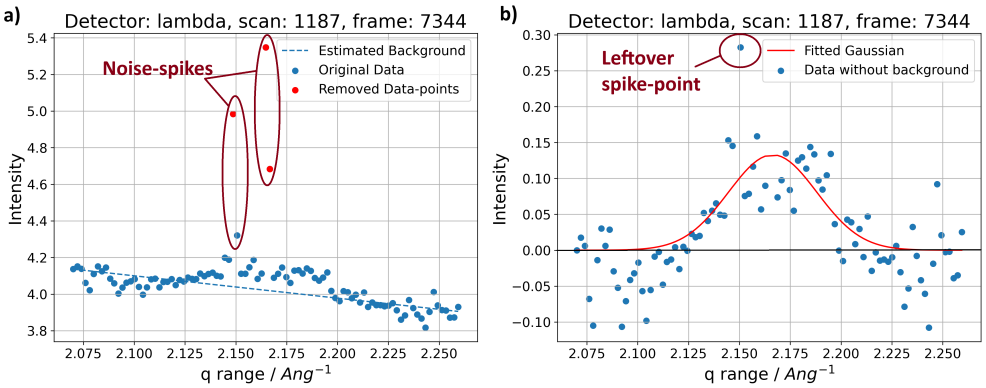


Figure 3.4: Example of a test-fit without the use of the gliding averaging method for a low/difficult peak with two arbitrary spikes where: a) showing the original data, the background-noise fit and spike points to be removed. b) showing a Gaussian-fit to the filtered data. The two combined shows the difficulty to get a perfect fit for all frames.

The script could be used for single-peak fitting for arbitrary frames which returned the average peak-position $q$, the Full Width at Half Max $FWHM = 2\sqrt{2log(2)}\sigma$ for the variance $\sigma$; the intensity $I = A\sigma\sqrt{2\pi}$ for the amplitude $A$; and the $R^2$ quality factor known as the coeffi-

cient of determination calculated according to,

$$R^2 = 1 - \frac{SS_{res}}{SS_{tot}} \tag{3.1}$$

$$SS_{res} = \sum_{i=1}^{n} (y_i - \hat{y}_i)^2 \tag{3.2}$$

$$SS_{tot} = \sum_{i=1}^{n} (y_i - \overline{y})^2, \tag{3.3}$$

for the Sum of Square of Residuals ($SS_{res}$) where $y_i$ is the actual observed value, $\hat{y}_i$ is the predicted value from the model; and for the Total Sum of Squares ($SS_{tot}$) where $\overline{y}$ is the mean of the observed values $y$.

From the data illustrated in fig. 3.4, the initial quality factor without applying the gliding averaging technique was $R^2_{noisy} = 0.56$, and the corresponding fitted peak value was $q_{noisy} = 2.16636$ Å$^{-1}$. Conversely, after smoothing the data using the gliding averaging method, the quality factor improved to $R^2_{smooth} = 0.77$, with the peak value refined to $q_{smooth} = 2.16640$ Å$^{-1}$.

By applying this analysis to various arbitrary frames and peaks, it was possible to establish a general threshold for the quality factor. This threshold was then used to iterate over all frames in a selected scan, thereby generating a dataset for mapping the sample. The dataset was then filtered based on the quality factor to exclude any unreliable fits characterized by low $R^2$ values.

Modifications to the script enabled it to work for data featuring two closely spaced peaks, aiming to resolve the desired superlattice peak-split. This adjustment involved creating a set of fitting variables for each peak, while the $R^2$ quality factor was derived from a dual Gaussian fit of both peaks combined. The derived parameters aided in the creation of separate plots for each peak, as combining them in a single plot was not practical.

Ultimately, the script was adapted to handle any data type presented, extracting the necessary fitting parameters for visualization. Consequently, a table was compiled to categorize each peak across the entire q-range from the WAXS dataset, covering both pre- and post-assembly scans.

### 3.4.2 Time-evolution of NCs self-assembly into MCs

*In situ* scans were conducted to monitor the self-assembly process of $CsPbBr_3$ NCs into MCs. Over a span of 1 hour, 8 minutes, and 30 seconds, a total of 26 scans (numbered 1155-1181) were performed, with an interval of approximately 2 minutes and 37 seconds between each scan. Each scan had a resolution of 81x50 (4050 pixels) with step sizes 25$\mu m$ and 100$\mu m$ (x,y) as previously described under section 3.2, which was slightly lower compared to the resolution of 51x240 (12240 pixels) with step sizes 50$\mu m$ and 25$\mu m$ used in the pre- and post-assembly scans.

To manage the WAXS data, where a single peak initially observed later evolved into a double peak, a method was necessary for the script to identify the type of peak present and accord-

ingly select the appropriate fitting approach. This involved hard-coding the ranges to search for different peaks, thus pressing the implementation of the gliding averaging function to prevent incorrect peak identification due to scattered points.

With this setup in place, the script could systematically process each scan, saving the necessary parameters for subsequent visualization. Additionally, an animation was created to depict the real-time positioning of the capillary and the intensity evolution throughout the period, illustrating how the NCs transitioned into MCs.

# 4 Results

## 4.1 Peak identification

With the completion of a script capable of fitting and extracting parameters from any peak of interest within the desired scans, it became possible to identify distinct peaks across the entire q-range of those scans. The integrated 1D data from the WAXS scans at the start of the experiment (pre-assembly, scan 1187) and at the end of the experiment (post-assembly, scan 1186) were utilized for this purpose. In both cases, individual frames representing signals from NCs in solution and from MCs were chosen in addition, in order to observe and illustrate more a detailed spectra.

An illustrative example of the integrated 1D data from scan 1187, paired with a chosen frame from scan 1186 that highlights distinct and labeled peaks, is presented in fig. 4.1. This figure shows the whole q-range with peaks ranging from the solvent and antisolvent, to different crystal planes, all identified by the method described in the following paragraphs. Information regarding the most interesting peaks can be found in tab. 4.1, while the summarized and cross-referenced values for all peaks can be found in Appendix A, tab. 7.1.

The integrated plot a) in fig. 4.1 was initially employed to identify ROIs for closer examination of each peak, similarly to the method illustrated in fig. 3.3. This plot, which aggregated data from multiple frames, was expected to yield the most accurate average peak parameter values. However, as the comparison between plot a) and b) of fig. 4.1 shows, some distinct difference in details, such as the $a_1$ peak from hexane and the initial peak of the superlattice at approximately $q \approx 1.08$ Å$^{-1}$, are obscured in the integrated data (similar issues are noted with the $a_2$ split into $b_1$ and $b_2$ occurring in the 1186 data). Consequently, plots of individual frames like plot b) were generated to provide a more detailed view of these peaks.

The integrated plot can be considered as if a large beam would hit the whole sample at the same time, thus loosing a lot of information. While individual frames such as fig. 4.1 b) provides information of a single point in the sample. When applying the scanning WAXS method with a small beam, where many single points are scanned in detail, very accurate maps of the capillary can be produced as will be seen later in the results.

This shows the relevance of the scanning XRD, as individual points in the sample can provide information that otherwise is lost for a whole sample scan, which the integrated data resembles.

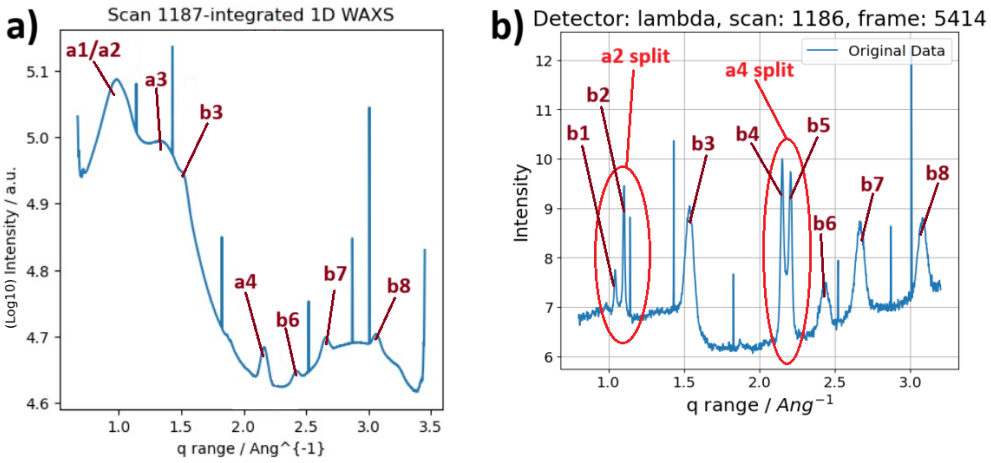


Figure 4.1: Labeled Peaks from Pre- and Post-Assembly WAXS Scans with visible noise-spike artifacts from the detector: a) displays the logarithmic integrated pre-assembly plot from scan 1187, primarily used for identifying the most distinguishable peaks. b) presents a chosen frame of prominent peaks from the post-assembly scan 1186, which reveals more distinct peaks and the peak splittings of the first-order split at $a_2$ and the second-order split at $a_4$ as seen in a). Notably, $a_2$ and its split was not distinguishable in the integrated plot, unlike $a_4$ as seen in fig. 3.3 a).

Table 4.1: Experimental and tabulated values for the most interesting of the labeled peaks in example fig. 4.1 from scans 1186 and 1187 (Peak "X"). The experimental (exp) q and d values for each peak were determined and cross-referenced to the values for $CsPbBr_3$ perovskite with orthorhombic crystal structure as determined by Rietveld refinement of the NC powder diffraction data, provided in the supporting information of Toso et al. [5]. These values were then compared to those depicted in Figure 1(c) of the same study.

| Peak "X" | q [Å$^{-1}$] (exp) | d [Å] (exp) | d [Å] (tab) | Plane (h k l) | Extra notations |
|---|---|---|---|---|---|
| $a_2$ | 1.08 | 5.81 | 5.8874 | (0 0 2) | Single peak from |
| | | | 5.83317 | (1 1 0) | 1187 frame 9735 |
| $b_1$ | 1.04 | 6.02 | Same as above | First order | First peak of $a_2$ split |
| $b_2$ | 1.10 | 5.71 | | Second order | Second peak of $a_2$ split |
| $a_4$ | 2.17 | 2.90 | 2.9437 | (0 0 4) | Single pre-assembly |
| | | | 2.91658 | (2 2 0) | peak from integrated |
| $b_4$ | 2.15 | 2.92 | Same as above | First order | First peak of $a_4$ split |
| $b_5$ | 2.20 | 2.85 | | Second order | Second peak of $a_4$ split |

## 4.2 WAXS second order superlattice analysis

### 4.2.1 Scan 1187 - Pre-assembly of mesocrystals

The focus of the analysis was on the second-order superlattice peak split of $a_4$ into the satellites $b_4$ and $b_5$ at $q \approx 2.17$ Å$^{-1}$, resulting from the alignment of the (004) and (220) crystal planes between adjacent NCs within the MCs. Therefore, the ROI was established around this peak, and the entire dataset from the pre-assembly scan 1187 of the replica sample was systematically looped through, fitted, and subsequently mapped. The intensity map, depicting the real position of the capillary and showing the concentration of the individual $CsPbBr_3$ NCs in C10 hexane solvent, is illustrated in fig. 7.1 located in Appendix A. The left side of fig. 4.2 a) from the *in situ* scans illustrates the same pre-assembly phase but for the non-replica sample with a bit lower resolution.

### 4.2.2 Scans 1155-1181 - *In situ* self-assembly process

*In situ* scans were conducted to observe the self-assembly of $CsPbBr_3$ NCs into MCs, which were then processed into an animation to illustrate the evolution of superlattice structures in the WAXS data. For obvious reasons, the animation could not be shown in this report, instead four semi-evenly distributed frames from the animation was put together into a figure which will be referenced as "the animation" for simplicity. These frames showed the intensity maps, similar to the pre-assembly scan shown in fig. 7.1, but for three individual peaks at each moment, the first split peak from the MC formation $b_4$, the single peak from free NCs mixed in hexane $a_4$, and the second split peak from the MCs $b_5$. These maps are displayed in fig. 4.2, which highlights the growth of mesocrystals as the intensities of the $a_4$ peak split into the satellites $b_4$ and $b_5$, as previously identified in fig. 4.1.

The frames in fig. 4.2 from the WAXS animation illustrates the gradual formation of superstructure MCs along the inner surface of the Kapton capillary, as they need to initially assemble onto a surface. As well as the simultaneous depletion of free NCs. The concentration of single NCs primarily clusters at the solvent-antisolvent interface, forming a pronounced ring. Additionally, a smaller, less dense ring of MCs is visible at the top of the capillary, both highlighted in red in the frames b) and d) respectively.

The $R^2$ quality factor used for filtering the animation scans was set to 0.8, and the frames was chosen up to scan 1175 as any later scans did not show any prominent improvements to the mesocrystal formation.

### 4.2.3 Scan 1186 - Post-assembly of mesocrystals

Following the completion of the *in situ* scan, a post-assembly scan (number 1186) was conducted at the higher resolution of 51x240 (12240 pixels), as previously explained in the method. This scan helped produce a more detailed intensity map of the capillary, specifically focusing on the split peaks $b_4$ and $b_5$. As depicted in fig. 4.3, this map shows the correlation between the two peaks, as the concentration of the separate Bragg-peaks are mirrored in the two separate maps. This indicates the reflection of the identical planes (004) and (220) of adjacent NCs in the MCs, at the same points in the capillary. The image also reveals an elevated intensity

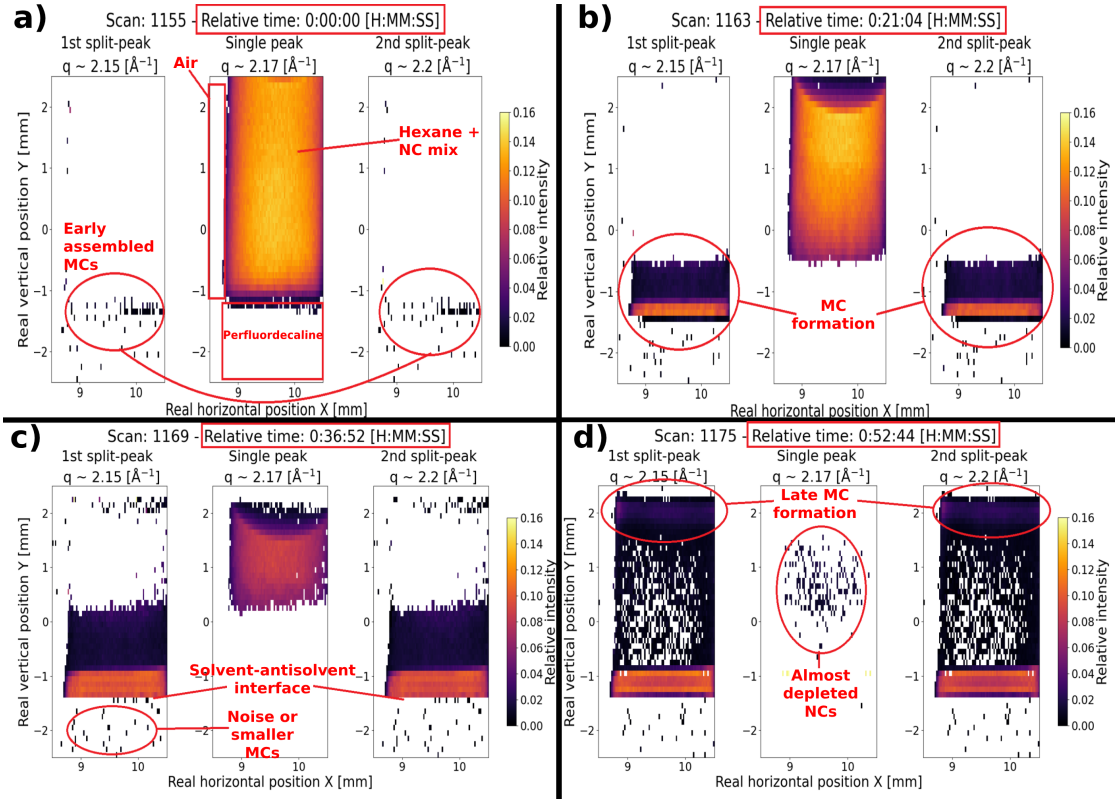


Figure 4.2: Four frames with the relative time at the top, from the *in situ* WAXS animation depicting the self-assembly process of MCs across scans 1155-1181. Each frame from a) to d) highlights the intensities of the $a_4$ peak as it divides into the satellites $b_4$ and $b_5$, as identified in fig. 4.1. The images also distinctly capture the mesocrystal formation, appearing more prominently at the bottom and less intensely at the top of the capillary at the end of the process. Higher intensity (brighter points) indicates a higher concentration of MCs.

at the edge of the mesocrystal formation along the interior of the capillary.

The pre-assembly scan 1187 was conducted after the post-assembly scan 1186 using a replica sample, which accounts for the later scan number. However, both scans were performed at the same resolution, contrary to the *in situ* scans (numbered 1155-1181).

Note, the vertical alignment differs by 1mm between scans 1186 and the *in situ* scans 1155-1181, although they analyzed the same sample. This misalignment probably occurred because scan 1186 was meant to be adjusted 1mm higher, but adjustments to scanning parameters inadvertently shifted the origin, altering where the crystals were observed, mainly noticeable by the main concentration of MCs (the ring) at $y = -1\,mm$ in the *in situ*, and $y = 0\,mm$ in the post-assembly plot.

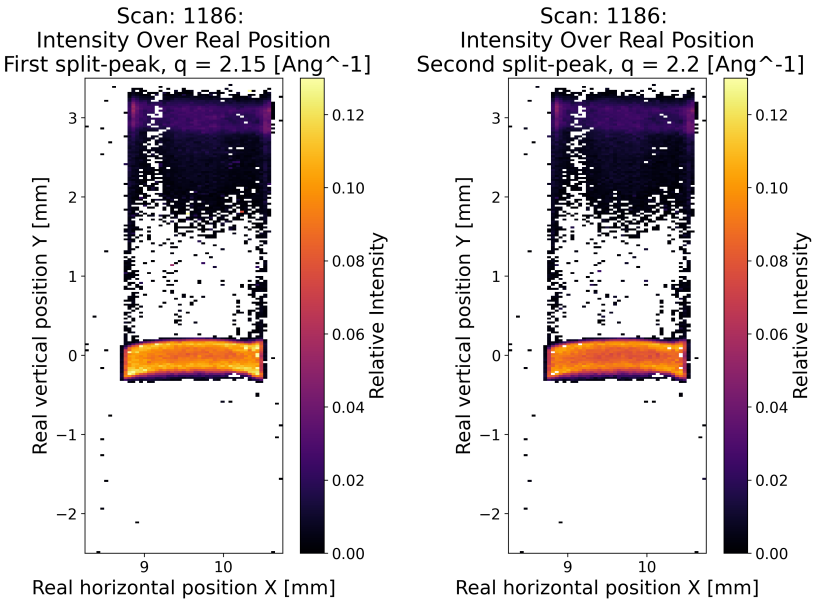


Figure 4.3: Post-assembly WAXS Scan 1186: This plot displays the detailed map of the Kapton capillary, highlighting the superlattice intensities for the split peaks $a_4$ into $b_4$ and $b_5$, as identified in fig. 4.1. The image captures the enhanced intensity regions at the edges where the mesocrystal formations are most concentrated, providing a clear view of the structural evolution within the capillary.

## 4.3 Complementary analysis of SAXS scan 1186

The SAXS data, captured at shorter angles, revealed the MC structures, with individual NCs diffracting similarly to atoms in a single crystal, comparable to observations made with WAXS.

### 4.3.1 The average nanocrystal distances

Using the expression following eq. 2.6, the distance between the centers of two NCs arranged in a superlattice could be determined as: $\Lambda = 2\pi n/q_n$. The q-value difference between the split peaks $b_4$ and $b_5$, as identified in tab. 4.1, is $q_{b5-b4} = 2.20 - 2.15$ Å$^{-1}$ = 0.050 Å$^{-1}$ with an estimated uncertainty of about 0.001 Å$^{-1}$, resulting in a calculated $\Lambda \approx 125.7$ Å with an estimated uncertainty of about 2.5 Å.

Additionally, with the integrated SAXS data, the average distance between NCs could be computed by initially fitting the prominent peak located at approximately $q \approx 0.06$ Å$^{-1}$, yielding an experimental value of $q_{SL} \approx 0.0603$ Å$^{-1}$. Subsequently, using eq. 2.5, the real space distance was computed to be $d_{SL} \approx 104$ Å.

### 4.3.2 Examining the SAXS peak- and intensity-map

Similar results to the WAXS data was made from the SAXS data, including an animation from the *in situ* scan and a comprehensive map of the post-assembly scan.

Fig. 7.2, found in Appendix A, presents the complete peak and intensity maps for the post-assembly scan 1186, focusing on a single peak at approximately $q \approx 0.06$ Å$^{-1}$. This intensity plot closely corresponds to the WAXS scan of the superlattice (SL) split peaks as seen in fig. 4.3. Additionally, the peak position map in this figure highlights variations across the sample, illustrating how the spacing between NCs within the MCs changes within the sample.

A specific section of the maps was examined in detail, as denoted by a red rectangle in both maps of fig. 7.2. This region was subsequently enlarged and depicted in fig. 4.4. The analysis primarily focused on the variation in peak position, which was investigated by moving upward along the y-axis at a fixed x-coordinate of 9 mm. In fig. 4.4, the left plot a) displays the variation in peak position and intensity relative to its location within the capillary, as shown on the left side of b). The areas highlighted in blue in b) indicate the most prevalent q-value corresponding to the area with the highest concentration of mesocrystals as seen when compared to the right side of b) that illustrates the intensity and thus concentration of the SL structures.

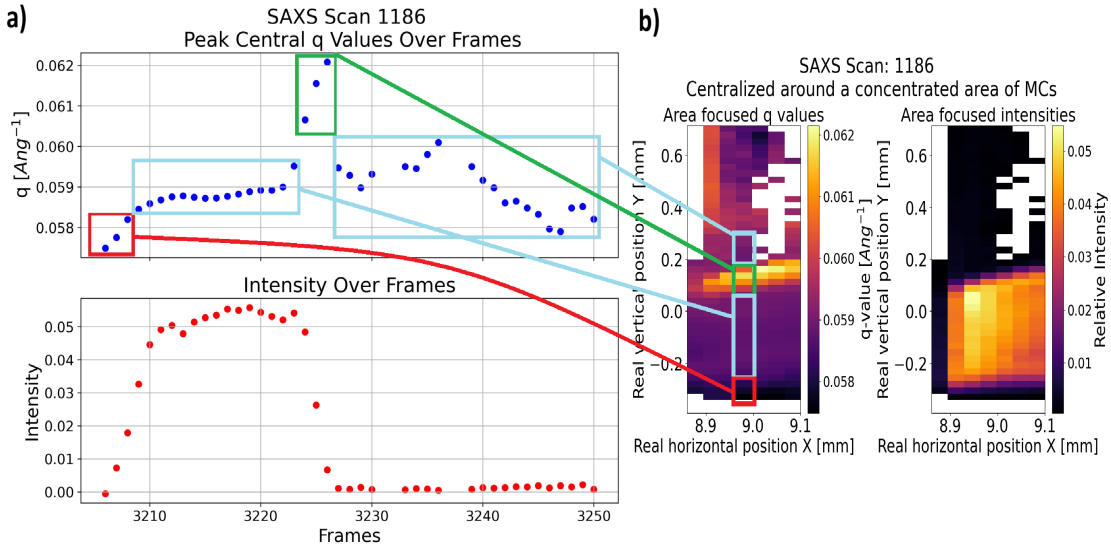


Figure 4.4: Examination of a selected range of frames from scan 1186. The focus being on variations in peak position and intensity along a fixed x-coordinate of 9 mm, moving upward on the y-axis over the main area of mesocrystal-formation. a) showing the central peak values q and intensities individually over each frame, where the q value plot also highlights in color the areas relative to the maps in b).

# 5 Discussion

## 5.1 Coding and data-handling difficulties

Developing a script to automatically process large datasets with uniform data structures is complex and includes a multitude of challenges. As noted in the method section, manually

inspecting frames or pixels across scans with 4000-12000 times 2000 data points each is impractical, but by instead making a general solution the fit quality might be compromised.

A major issue in data processing is the removal of background noise and interference, particularly with varied spectral features like different peak shapes and noise spikes. Fig. 3.4 illustrates a problematic frame. Addressing noise spikes is relatively straightforward by analyzing derivatives between adjacent points. However, removing background noise is more complicated. For WAXS data, a simple linear fit using the average of the first and last 10 points generally suffices for well-defined peaks, but lower, noisier peaks often result in inaccurate parameter estimation due to improper background subtraction.

Improvements could include doing the moving averaging prior to removing the background as the opposite was done in this analysis. Using a broader range of points for averaging or focusing on the lowest points to minimize the impact on larger peaks. Alternatively, methods like the second-degree polynomial fit or the "Rolling ball" algorithm were tested; the former proved effective for SAXS data with nonlinear backgrounds, balancing simplicity and accuracy.

The introduction of the gliding averaging method later in the project significantly improved fit quality. Initially overlooked due to seemingly adequate data quality, its integration greatly enhanced the precision of fits, as demonstrated by the improvement in the quality factor of Gaussian fits from $R^2_{noisy} = 0.56$ to $R^2_{smooth} = 0.77$ in fig. 3.4. This underscores the method's value in refining data analysis, especially in handling large and complex datasets.

## 5.2 Analysis of peaks and images

### 5.2.1 Peak identification

In identifying the peaks as shown and labeled in fig. 4.1, the precision of the parameter values subsequently used to fill tabs. 4.1 in the results, and 7.1 in Appendix A was not emphasized. Specifically, the values for the first-order split peaks ($a_2$ into the satellites $b_1$ and $b_2$) were derived from individual fits of a single frame rather than from averages across multiple frames. Given time constraints, a rough estimation was deemed sufficient for the initial identification of each peak, with more detailed analyses reserved for peaks of particular interest later in the study. This approach also explains the reliance on integrated plots, which provided a straightforward and quick average value for peak positions by directly accounting for all frames.

Due to this prioritization of efficiency over precision, identifying each peak as recorded in the two tables proved challenging. The uncertainty, or errors for the experimental values was only reliable for the first decimal place. A more uniform approach, potentially averaging multiple frames and including metrics such as the average width or Full Width at Half Maximum (FWHM) of the peaks, could have helped with a more accurate determination of the crystal planes associated with each peak.

Fortunately, the study by Toso et al. [5] provided not only the tabulated values for the interplanar distances "d", and their corresponding crystal planes for cross-referencing, but also a detailed illustration (Figure 1c) of the Miller indices for the six most intense reflections related

to the Bragg peak for randomly oriented NCs. This additional information was invaluable for validating and refining our peak identification process.

### 5.2.2 Comparing the WAXS intensity maps

The findings from the WAXS data primarily focused on the second-order superlattice peak split of $a_4$ into its satellite peaks, corresponding to the (004) and (220) crystal planes.

The intensity map in fig. 7.1 from the pre-assembly replica sample (scan 1187) highlights a radial and vertical decrease in NC concentration within the capillary. The radial decrease is due to the longer path the incoming beam travels in the center compared to the edges of the cylindrical capillary. The less apparent vertical decrease may be influenced by the timing differences in experimental setup and filling techniques, potentially allowing NCs more time to blend with the neat hexane layer, reducing intensity near the solvent-antisolvent interface. This is suggested by the comparison between the two pre-assembly phase scans, 1155 as seen in fig. 4.2 a), and the 1187 scan as seen in fig. 7.1, where the same intensity pattern is not observed for the two separate samples.

Differences in filling techniques and the precise dosing required, in addition to the the scanning resolutions, could also contribute to variability in intensity patterns. *In situ* scans, with a resolution of 4050 pixels and larger step sizes, contrast with the finer 12240 pixel resolution of the pre- and post-assembly scans. This variation affects how intensities are distributed and perceived across the capillary.

When studying the evolution of the assembly process from the four frames of the *in situ* animation as depicted in fig. 4.2, one can conclude that the MCs deposit onto the capillary walls at the solvent-antisolvent interface and then grows upwards along the inner walls. The smaller amount of MCs is also observed at the top of the capillary which might be an effect of some capillary flow of the NC solution occurring during the process, perhaps caused by the partial evaporation of the hexane, as the capillary is not capped.

The self-assembly process completed in about one hour, with minimal changes observed from the last frame in fig. 4.2 d) to scan 1181, suggesting that most of the the free NCs have assembled into MCs, as confirmed by the high-resolution post-assembly scan in fig. 4.3. Early signs of MC formation were apparent within just five minutes from the start in scan 1157, demonstrating the hexane solvent interlayer's crucial role in the initiating assembly.

By 21 minutes, as seen in fig. 4.2 b), a foundational layer of MCs had formed. Sixteen minutes later, fig. 4.2 c) shows a significant decrease in free NCs, indicated by reduced intensity in central plots as time evolves.

## 5.3 The Superlattice

As calculated in the results, the distance between the satellite peaks from the $a_4$ split was $q_{b5-b4} = 2.20 - 2.15$ Å$^{-1}$ = 0.050 Å$^{-1}$, resulting in a calculated $\Lambda \approx 125.7$ Å. This value agrees fairly well with $\Lambda_{replica} = 127$ Å from the WAXS multilayer diffraction analysis done in Italy, on a sample made from replica nanocrystals, as to be presented in the paper in preparation, Filippi et al. [8]. Additionally, with the integrated SAXS data, the average q value between NCs

could be computed to be $q_{SL} \approx 0.0603$ Å$^{-1}$, resulting in the real distance to be $d_{SL} \approx 104$ Å.

The first two values from the separate WAXS analysis of the satellite peaks ($\Lambda = 125.7$ Å and $\Lambda_{replica} = 127$ Å), as mentioned agreed well with each other, while the SAXS data provided a shorter distance of $d_{SL} \approx 104$ Å. This could be a real difference caused by the differences in how SAXS and WAXS signals originate. As we are working with orthorhombic $CsPbBr_3$ perovskites, if the crystal planes causing the peak split in the WAXS data are perpendicular to the elongated sides of the perovskites, then the distance would be longer between the two planes than for the SAXS data which looks at the NCs as individual electron bunches. This difference in distance between the SAXS and WAXS data is undetermined and thus should be investigated further.

Additional analysis of the SAXS data, particularly focusing on the area marked in red as shown in fig. 7.2 (found in Appendix A), reveals variations in NC distances at different stages of MC formation. This specific area is elaborated in fig. 4.4 b), while fig. 4.4 a) provides detailed value differences. It's important to note that real space distance is inversely related to the q value, meaning a higher q value corresponds to a shorter distance between NCs within MCs. The observed higher intensity in fig. 4.4 suggests denser MC packing. Comparatively, this indicates longer distances between NCs at the brighter upper edge of the MC formation and shorter distances at the darker lower edge. Combined with the general MC formation observed in fig. 7.2, these findings suggest that the distribution and spacing of NCs within MCs vary along the capillary, indicative of a density-dependent structuring that affects the mesostructure properties.

An intriguing observation emerges from examining the upper ring of MCs in fig. 7.2 and comparing the two plots. The variation in q intensity reflects the distribution of MCs within the sample and the differences in q values indicate varying periodicities among the MCs. This variation could be due to size segregation, as the initial NCs in solution typically have a size distribution of $\pm 0.5 - 1$ nm, or it could be influenced by the size of the MCs themselves, with larger MCs appearing more "compressed" than smaller ones.

# 6 Conclusions and outlook

The data analysis methods developed in this thesis and the results obtained from *in situ* experiments has improved our understanding of the process of NC self-assembly at the solvent-antisolvent interface. New information about the self-assembly dynamics and structural characteristics of the cesium lead bromide ($CsPbBr_3$) NCs into MCs has been found using *in situ* scanning SAXS/WAXS techniques. The study demonstrated that the distribution and spacing of NCs within MCs are density-dependent, affecting the overall mesostructure properties. To highlight that before this experiment we assumed that all MCs formed via this process are alike, and in this experiment we actually observed that it is not the case.

This challenges implicit assumptions of uniformity of MCs formed in self-assembly process and suggests that controlling the environment and conditions of NC assembly could lead to reproducible nanomaterials with more predictable and tailored properties. The use of scanning SAXS and WAXS has proven effective for real-time, *in situ* measurements, providing a

suitable method that can be applied to other research in nanomaterials.

Additional findings reveal notable differences in the distances measured between NCs, with SAXS indicating a closer inter-NC distance ($d_{SL} \approx 104$ Å) compared to WAXS, which showed a larger spacing ($\Lambda \approx 125.7$ Å) due to the measurement of the planes between adjacent NCs that is known as the superlattice split. The reason for this difference is unconcluded and requires a deeper investigation in order to fully understand this outcome. This discrepancy underscores the complexity of the mesostructures and the importance of using complementary techniques to capture the full scope of nanoassembly dynamics.

Although this project was not directed towards any specific technological applications, the methods developed and the information gained are promising to be beneficial for the broader field of material science, particularly for understanding the self-assembly processes of nano-sized building blocks dispersed in a liquid. That could be relevant for processes like biomineralization, protein crystallization, and soft-matter in general. For me, the author, this thesis has significantly improved my skills in data handling and background processing, helping me develop the analytical capabilities as presented in this thesis. These learning outcomes have given me a useful toolbox for data analysis and visualization of in situ scattering data. Allowing me the opportunity to do more complex analyses in future research.

This research is a new step into the understanding of the self-assembly mechanisms at play. A more detailed investigation into the physical-chemical interactions within the assembly process could provide valuable information about the forces driving NC alignment and attachment. Future studies could include topics like, kinetics, i.e. characterizing the timescales of MC growth and coarsening (changes in NC separations over time). And comparison to MC growth from NCs with different surface molecules, as the experiment conducted in this thesis also included measurements of samples with similar NCs but covered with longer ligands. Hence the method of data analysis developed here could be used to learn how different NC surface changes MC growth. Furthermore, to include the optoelectronic properties of the assembled structures could link structural attributes to functional outcomes, beneficial for applications in photovoltaics, sensors, and other electronic devices.

In conclusion, this thesis provides new information and understandings about the *in situ* analysis of perovskite NC self-assembly into MCs. Additionally, it shows how effective scanning XRD can be on these types of real-time experiments on nanoscaled material, and what great potential it could have on any future research. Furthermore, it can help in setting the groundwork for new research within the field of perovskite MCs, which has been a hot topic in the scientific community as of late.

## References


[1] E.V. Sturm (née Rosseeva), H. Cölfen, Chem. Soc. Rev. **45**, 5821 (2016), **DOI** 10.1039/C6CS00208K

[2] Z. Mohammed, S. Sami, J. Salih, East European Journal of Physics pp. 263–270 (2023), **DOI** 10.26565/2312-4334-2023-3-23

[3] S.T. Ha et al., Chem. Sci. **8**, 2522 (2017), **DOI** 10.1039/C6SC04474C

[4] W. contributors, *Bravais lattice — Wikipedia, the free encyclopedia* (2024), [Online; accessed 26-March-2024], https://en.wikipedia.org/w/index.php?title=Bravais_lattice&oldid=1213589128

[5] S. Toso et al., ACS Materials Letters **1**(2), 272 (2019), pMID: 32954357, https://doi.org/10.1021/acsmaterialslett.9b00217, **DOI** 10.1021/acsmaterialslett.9b00217

[6] M.A. Boles, M. Engel, D.V. Talapin, Chemical Reviews **116**(18), 11220 (2016), pMID: 27552640, https://doi.org/10.1021/acs.chemrev.6b00196, **DOI** 10.1021/acs.chemrev.6b00196

[7] O.H. Seeck, B. Murphy, eds., *X-Ray Diffraction: Modern Experimental Techniques*, 1st edn. (Jenny Stanford Publishing, New York, 2014), ISBN 9780429071898, published on 13 February 2015

[8] U. Filippi et al. (2024), manuscript in preparation

[9] D. Baranov et al., The Journal of Physical Chemistry Letters **10**(3), 655 (2019), pMID: 30676762, https://doi.org/10.1021/acs.jpclett.9b00178, **DOI** 10.1021/acs.jpclett.9b00178

[10] MAX IV Laboratory, *Formax*, https://www.maxiv.lu.se/beamlines-accelerators/beamlines/formax/, accessed: 2024-04-09

[11] Jensen, Alexander Bernthz and Christensen, Thorbjørn Erik Køppen and Weninger, Clemens and Birkedal, Henrik, **29**, 1420 (2022), ISSN 1600-5775, **DOI** 10.1107/S1600577522008232

[12] pyFAI Contributors, *Fast azimuthal integration using python*, https://pyfai.readthedocs.io/en/v2023.1/ (2023), accessed: 2024-04-09

# 7 Appendix A

The experimental and tabulated values from Toso et al. [5] for all of the peaks identified and labeled in fig. 4.1 can be found tab. 7.1 below.

Table 7.1: Experimental and tabulated values for the labeled peaks in example fig. 4.1 from scans 1186 and 1187 (Peak "X"). The experimental (exp) q and d values for each peak were determined and cross-referenced to the values for $CsPbBr_3$ perovskite with orthorhombic crystal structure as determined by Rietveld refinement of the NC powder diffraction data, provided in the supporting information of Toso et al. [5]. These values were then compared to those depicted in Figure 1(c) of the same study.

| Peak "X" | q [Å$^{-1}$] (exp) | d [Å] (exp) | d [Å] (tab) | Plane (h k l) | Extra notations |
|---|---|---|---|---|---|
| $a_1$ | 0.98 | 6.42 | | | Perfluorodecalin |
| $a_2$ | 1.08 | 5.81 | 5.8874 | (0 0 2) | Single peak from |
| | | | 5.83317 | (1 1 0) | 1187 frame 9735 |
| $b_1$ | 1.04 | 6.02 | Same as above | First order | First peak of $a_2$ split |
| $b_2$ | 1.10 | 5.71 | | Second order | Second peak of $a_2$ split |
| $a_3$ | 1.34 | | | | Hexane |
| $b_3$ | 1.53 | 4.11 | 4.14371 | (1 1 2) | Peak from |
| | | | 4.13705 | (0 2 0) | 1187 frame 9735 |
| | | | 4.1124 | (2 0 0) | |
| $a_4$ | 2.17 | 2.90 | 2.9437 | (0 0 4) | Single pre-assembly |
| | | | 2.91658 | (2 2 0) | peak from integrated |
| $b_4$ | 2.15 | 2.92 | Same as above | First order | First peak of $a_4$ split |
| $b_5$ | 2.20 | 2.85 | | Second order | Second peak of $a_4$ split |
| $b_6$ | 2.42 | 2.60 | 2.62802 | (1 1 4) | Peak from integrated |
| | | | 2.61493 | (1 3 0) | |
| | | | 2.61347 | (2 2 2) | |
| | | | 2.60246 | (3 1 0) | |
| $b_7$ | 2.65 | 2.37 | 2.39849 | (0 2 4) | Peak from integrated |
| | | | 2.39366 | (2 0 4) | |
| | | | 2.38981 | (1 3 2) | |
| | | | 2.38028 | (3 1 2) | |
| | | | 2.34101 | (2 2 3) | Close in range |
| $b_8$ | 3.06 | 2.05 | 2.07186 | (2 2 4) | Peak from integrated |
| | | | 2.06853 | (0 4 0) | |
| | | | 2.0562 | (4 0 0 ) | |
| | | | 2.04661 | (0 2 5) | |
| | | | 2.03733 | (0 4 1) | |

Fig. 7.1 illustrates the pre-assembly scan 1187 made with the higher resolution of 12240 pixels over a 2.5x6 mm range with step sizes 50$\mu m$ and 25$\mu m$ respectively (x,y). The data

underwent filtering based on an $R^2$ quality factor threshold of 0.2. Additionally, the sample analyzed was a replica of those used in the *in situ* scans 1155-1181 and post-assembly scan 1186.

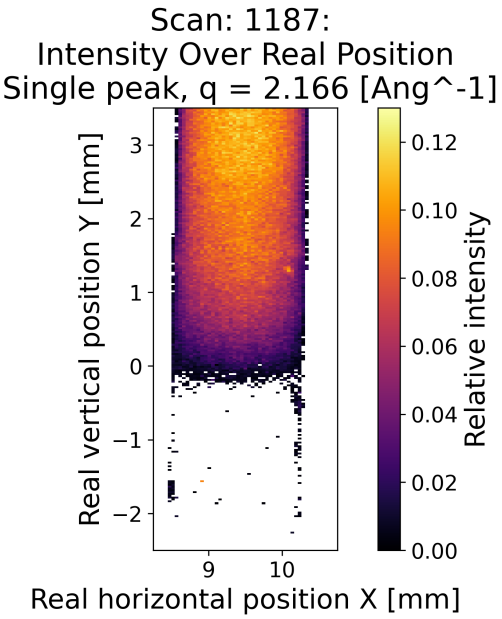


Figure 7.1: Pre-assembly WAXS Scan 1187: The plot illustrates the intensity mapping relative to the actual position of the Kapton capillary, showing the localization of lead halide perovskite nanocrystals (LHP NCs) around the distinct single peak $a_4$ with peak center at $q \approx 2.17$ Å$^{-1}$.

Fig. 7.2 illustrates the complete SAXS peak and intensity maps for the post-assembly scan 1186, mainly produced in order to partly show the different NC distances in the MCs formed around the capillary. But also to focus on a specific section of the maps as denoted by a red rectangle in both maps. This region was subsequently enlarged and depicted in fig. 4.4 where it was studied in more detail.

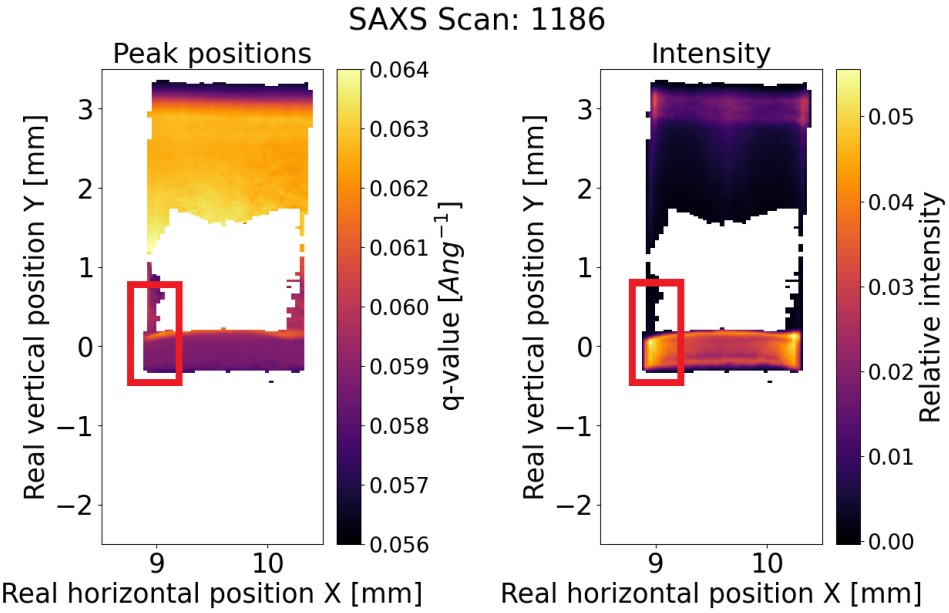


Figure 7.2: Post-assembly SAXS peak and intensity maps for scan 1186: This figure illustrates the detailed maps of a single peak at approximately $q \approx 0.06\,\text{Å}^{-1}$ in the SAXS data, reflecting similar structural delineations as the WAXS split peaks shown in Figure 4.3. Both plots have areas highlighted with red rectangles that are further studied in fig. 4.4.

# 8 Acknowledgments

First of all, I would like to say many thanks my supervisor, Dr. Jesper Wallentin of the Division of Synchrotron Radiation Research for not only guiding me throughout this extremely exhausting journey, but also for allowing me to join him and his team on multiple beamtime experiments at MAX IV, which has been a lot of fun and educational. In his team I must also thank his PhD student Huaiyu Chen for giving me all the tools needed to get the project going and rolling, and his postdoc Megan Hill for giving me tips and explaining concept throughout the long work.

Secondly a huge thanks must be given to Dr. Dmitry Baranov, Division of Chemical Physics and NanoLund, Lund University, who were the one responsible for the whole project and allowing me to be a part of it. But who has also been frequently aiding me from the beginning to the end with understanding what actually is going on.

Additionally I would like to thank Mr. Umberto Filippi, IIT Genova, for synthesis and characterization of $CsPbBr_3$ perovskite NC samples. And his colleague Stefano Toso for answering my questions both during the beamtime and after, and for his paper that is used for references multiple times throughout the thesis.

We acknowledge MAX IV Laboratory for time on Beamline ForMAX under Proposal 20230363. Research conducted at MAX IV, a Swedish national user facility, is supported by the Swedish Research council under contract 2018-07152, the Swedish Governmental Agency for Innovation Systems under contract 2018-04969, and Formas under contract 2019-02496. The experiment was supported in part by the ERC Starting Grant Prometheus, project number 101039683.

OpenAI's ChatGPT was used for this thesis as an aid for both troubleshooting the code used for the analysis, as well as for spellchecking and shortening the text in general. Specifically, regarding the code, ChatGPT was used in order to solve potential error-messages that occasionally occurred, such as an incorrectly used variable, or incorrect use of syntax. In regards to the text, ChatGPT was used in order to get rid of unnecessary wordings that is commonly occurring in the first drafts of a report, in order to get a better flow in the text. Additionally, it was used in order to shorten parts of the text by removing unnecessary words, for the sake of retaining the set page limit of the thesis. This was mostly done in section 2 (Theory) and section 3 (Experimental Setup & Method), as they easily got very wordy when trying to explain the content in my own words. In other parts of the thesis it was used sporadically for minor textual revisions.

Special thanks to Friedlieb Ferdinand Runge for the discovery of caffein, and of course Gibban, you two are the real MVP's.

Finally, of course, thank you to all of my friends who has made this whole bachelor program possible. Everyone who has been in the Hole since day one, HKS and obviously Pub Rydberg's (because we all need a break once in a while). Anyone who has interacted with me at any time during these years, you have help me get through this difficult road, and I salute you.